PNAS RESEARCH ARTICLE | EARTH, ATMOSPHERIC, AND PLANETARY SCIENCES OPEN ACCESS

Dislocation theory of steady and transient creep of crystalline solids: Predictions for olivine

Thomas Breithaupt[a,b,1], Richard F. Katz[b], Lars N. Hansen[c], and Kathryn M. Kumamoto[c,d]

Edited by Peter Kelemen, Lamont-Doherty Earth Observatory, Palisades, NY; received February 25, 2022; accepted December 5, 2022

In applications critical to the geological, materials, and engineering sciences, deformation occurs at strain rates too small to be accessible experimentally. Instead, extrapolations of empirical relationships are used, leading to epistemic uncertainties in predictions. To address these problems, we construct a theory of the fundamental processes affecting dislocations: storage and recovery. We then validate our theory for olivine deformation. This model explains the empirical relationships among strain rate, applied stress, and dislocation density in disparate laboratory regimes. It predicts the previously unexplained dependence of dislocation density on applied stress in olivine. The predictions of our model for Earth conditions differ from extrapolated empirical relationships. For example, it predicts rapid, transient deformation in the upper mantle, consistent with recent measurements of postseismic creep.

dislocation creep | transient creep | dislocation density | olivine | Bauschinger effect

Significance

Many important deformation processes take place at strain rates that are too slow to be investigated experimentally. For example, strain rates in Earth's mantle are typically ten orders of magnitude slower than in the laboratory. To bridge this gap, empirical relationships are extrapolated with large epistemic uncertainties. We propose a model for deformation derived from the microphysics of deformation. In application to olivine, the main mineral of Earth's upper mantle, this model explains the scaling relationships observed under a range of laboratory conditions. In extrapolation to Earth's mantle, the model predicts a transition in the dominant microphysical processes, leading to predictions distinct from previous studies. For instance, following abrupt stress changes, it predicts rapid transient deformation.

Many problems in the materials, engineering and geosciences require assessment of the mechanical behavior of crystalline solids at extremely low strain rates. These include applications to gas turbines (1), power stations (2), glaciers (3), and Earth's interior (4). Understanding the mechanical properties of materials in these settings is crucial for predicting the creep-limited lifetime of engineering components and the response of the solid Earth to changing surface loads, such as shrinking ice sheets. The small strain rates in these settings are impractical or impossible to explore in laboratory experiments. Therefore, predictions are typically made by extrapolation from experiments performed at much higher strain rates. Confidence in such extrapolations should be based on a clear understanding of the physics of deformation. However, steady-state deformation data are largely rationalized using phenomenological power-law fits (5), and transient strain rates are often modeled using approaches that are not rooted in the underlying physics (6). At this point, there is no physics-based model of steady-state and transient deformation that is self-consistent across multiple deformation regimes.

Deformation of crystalline solids occurs by the motion of crystal defects. In this study, we examine the role of line defects—dislocations—within the crystal lattice. Deformation as a consequence of dislocation motion has been divided into categories including low-temperature plasticity, dislocation creep, and grain-size–sensitive dislocation creep, each of which has been modeled as a physically distinct mechanism, e.g., ref. 7. Going beyond these models of steady-state creep, the evolution of dislocation microstructure controls transient strain rates at low strains (8) and other classical features of deformation such as the Hall–Petch effect (9) and the Bauschinger effect (10). Here, we present a unified, physics-based, quantitative description of all these features of deformation associated with dislocation motion.

Deformation due to dislocation motion is sensitive to the density of dislocation lines within crystals. We therefore construct a model for evolution of dislocation density that makes physics-based, testable predictions about deformation at both low and high strain rates. The classical theory for dislocation-density evolution in the materials sciences is the Kocks–Mecking–Estrin (KME) model, which has been used to model low-temperature deformation of metals including silver, copper, aluminum, and nickel (11–16). This theory is derived from the hypothesis that dislocation density increases due to dislocation storage, a geometric description of the increase in dislocation-line length during dislocation glide, and decreases due to dynamic recovery, a description of strain-dependent dislocation annihilation that is thought to dominate at low temperatures (17). However, extensions of the KME model to high temperatures are problematic because they exclude key aspects of dislocation physics, incorporating either phenomenological parameterizations (12, 14) or relying on an empirical scaling between the applied stress and dislocation density (5, 18).

Author contributions: T.B., R.F.K., L.N.H., and K.M.K. designed research; T.B. performed research; T.B. analyzed data; and T.B., R.F.K., L.N.H., and K.M.K. wrote the paper.

The authors declare no competing interest.

This article is a PNAS Direct Submission.

[1]To whom correspondence may be addressed. Email: tpb44@cam.ac.uk.

This article contains supporting information online at http://www.pnas.org/lookup/suppl/doi:10.1073/pnas.2203448120/-/DCSupplemental.

Published February 13, 2023.

We demonstrate that laboratory data from experiments at low and high temperatures can be explained in a self-consistent manner by accounting for two additional aspects of dislocation physics. First, we augment the KME theory with a model for static recovery that describes the high-temperature, time-dependent annihilation of dislocations. In this model, we emphasize the role of fast-diffusion pathways in dislocation annihilation. Second, we couple the theory of dislocation evolution to a flow law that explicitly describes the competing roles of dislocations as both carriers of deformation and generators of stress fields that act to oppose deformation. The combined model provides a parsimonious, physics-based explanation of i) yield stresses at low temperatures, ii) steady-state and transient creep at high temperatures, iii) the scaling between dislocation density and stress, iv) kinematic hardening, v) the Bauschinger effect, and vi) the Hall–Petch effect.

All of these processes and phenomena are relevant to olivine (6, 7, 10, 19), a mineral that controls the strength of Earth's upper mantle. Olivine has four key advantages in testing our approach. First, its dislocation density can be readily measured using an oxidation-decoration technique (20), and there are many published experiments against which to compare model predictions (19, 21–23). Second, no physics-based model has self-consistently explained the scaling of the steady-state dislocation density with applied stress in olivine, which is empirically distinct from the classical case in which dislocation density is proportional to the applied stress squared (19). Third, recent experiments have demonstrated the crucial importance of modeling dislocation physics in understanding olivine deformation (6, 10), but currently, no self-consistent, physics-based model exists for this purpose. Fourth, there are a variety of independent geophysical observations that constrain the behavior of Earth's upper mantle at natural strain rates, e.g., refs. 4 and 24 that may eventually be used as a test of predictions of our model for strain rates inaccessible in the laboratory.

Model Derivation

The two essential components of our model are an equation for the evolution of dislocation density and a flow law that describes how strain rate depends on dislocation density and other variables, such as applied stress. Both are outlined here and detailed in *SI Appendix*, Text. Within our framework, we do not distinguish between different types or categories of dislocations.

Dislocation density, ρ, evolves due to dislocation storage and dislocation recovery. Dislocation storage describes the increase in ρ with increasing plastic strain as dislocation loops expand. The storage rate is $\dot{\varepsilon}/(bL)$, where $\dot{\varepsilon}$ is the strain rate, b is the magnitude of the Burgers vector, and L is a length scale that describes the average distance traveled by a dislocation before it is stored in the lattice (16). We assume that L is controlled by the presence of other dislocations and grain boundaries (*SI Appendix*, Text).

Dislocation recovery describes the decrease in ρ due to dislocation annihilation. Recovery may be characterized as dynamic, whereby its rate is strain-dependent, or as static, whereby its rate is time-dependent. Our model incorporates both types of recovery (*SI Appendix*, Text); to focus on unique aspects of the model and make connections with high-temperature creep data, we discuss only static recovery here.

In static recovery, dislocations of opposite sign are driven to climb and annihilate by the interaction of their stress fields (25). The rate of recovery depends on the amount of suitable dislocations, their separation, and the climb velocity (25). Dislocation climb requires diffusion of vacancies to the climbing segment of the dislocation. Classical treatments, which assume that vacancies diffuse through the lattice, suggest that the recovery rate is proportional to ρ^2 (25). However, vacancies can also diffuse along fast diffusion pathways, like dislocation cores and grain boundaries (26, 27). We focus on the role of these fast diffusion pathways and neglect diffusion through the bulk lattice (*SI Appendix*, Text). To account for different types of pathways, the diffusivities of each type are weighted by the volume fraction of that pathway (28). The volume fraction of dislocation cores (pipes) is proportional to ρ, and hence, the rate of recovery controlled by pipe diffusion is proportional to ρ^3. In contrast, the volume fraction of grain boundaries is inversely proportional to the grain size d, and thus, the rate of recovery controlled by grain-boundary diffusion is proportional to ρ^2/d.

Accounting for the rates of dislocation storage and static recovery, the evolution of dislocation density is given by

$$\dot{\rho} = \underbrace{\frac{1}{b}\left(m\sqrt{\rho} + \frac{n}{d}\right)\dot{\varepsilon}}_{\text{storage}} - \underbrace{\left(\mathcal{R}_{\text{gb}}(T)\frac{\rho^2}{d} + \mathcal{R}_{\text{pipe}}(T)\rho^3\right)}_{\text{static recovery}}, \quad [1]$$

where $\dot{\varepsilon}$ is the strain rate, m and n are material constants, T is the temperature, and $\mathcal{R}_{\times}(T)$ are rate coefficients for static recovery by grain boundary or pipe diffusion. The Arrhenius temperature dependence of these rate coefficients is associated with the diffusivity of the slowest-diffusing species along the respective pathway.

Eq. **1** is coupled to a flow law that describes the dependence of the strain rate on dislocation density, applied stress, and temperature. Dislocations are the carriers of deformation, so the flow law depends on dislocation density and velocity (29). Dislocation motion is a thermally-activated process (30) described by a stress-dependent energy barrier (*SI Appendix*, Text), which leads to the flow law

$$\dot{\varepsilon} = A(T)\rho \sinh\left(\frac{\sigma - \sigma_\rho - \sigma_d}{\sigma_{\text{ref}}(T)}\right), \quad [2]$$

where $A(T)$ is a rate coefficient with an Arrhenius dependence on temperature, and σ is the applied stress. $\sigma_{\text{ref}}(T)$ is the reference stress, which is related to the strength of barriers to dislocation motion and has a linear dependence on temperature (*SI Appendix*, Text).

Through thermodynamic considerations, we find that the applied stress is opposed by two microstructurally-derived stresses, σ_ρ and σ_d (*SI Appendix*, Text). The classical Taylor stress, $\sigma_\rho = \alpha\mu b\sqrt{\rho}$, describes the cumulative effect of stress fields generated by dislocations (31). Here, μ is the shear modulus, and α is a constant. The second, $\sigma_d = \beta\mu b/d$, is the threshold stress, which classically represents the minimum applied stress required for a dislocation loop to expand within a grain (32), where β is a constant. In traditional models of dislocation creep, the dislocation velocity is assumed to be limited by the timescale of dislocation climb, e.g., ref. 33. In contrast, within our framework, we self-consistently model the effect of dislocation climb on dislocation velocity through its influence on dislocation density. Slower dislocation climb leads to a higher dislocation density, and therefore a higher Taylor stress, which opposes the applied stress driving deformation in Eq. **2** and thereby limits the dislocation velocity.

Eq. **1** and Eq. **2** constitute our model for deformation due to dislocations at high temperatures. The model incorporates the

physics of both dislocation climb, through the recovery terms in Eq. **1**, and dislocation glide, in the form of the flow law Eq. **2**. The full model, detailed in *SI Appendix*, Text, self-consistently describes transient and steady-state deformation at both low and high temperatures and incorporates grain-size effects. Given the applied stress, temperature, and grain size, these equations can be solved for the evolution of dislocation density and strain rate, both prior to and at steady state.

Model Validation and Calibration

Before the model can be applied, it must be calibrated and validated by comparison with data derived from deformation experiments. To this end, we use published data from steady-state (Fig. 1) and transient (Fig. 2) creep experiments on olivine.

At steady state, the model predicts a (nonlinear) relationship among stress, dislocation density, and strain rate. This relationship is modulated by the grain size that, for simplicity, we treat as an independent variable, though in fact grain-size evolution may be coupled to dislocation density, e.g., ref. 36. We do not consider oxygen fugacity, which is known to affect strain rates (34). Since fugacity varies among experiments, we consider only data collected at the Ni–NiO buffer. Our calibration and subsequent extrapolation to mantle conditions are not particularly sensitive to differences among activation energies of different processes; we therefore assume that all temperature-dependent processes have the same activation energy, Q.

We first test the hypothesis that pipe diffusion plays a critical role in grain-size insensitive dislocation creep in olivine. To do so, we assume that grain-boundary diffusion is negligible and calibrate our model against the steady-state experimental data on large-grained (0.9 mm) aggregates from Keefner et al. (34). This calibration constrains the rate coefficients of the flow law Eq. **2** and pipe-diffusion recovery Eq. **1**, as well as the activation energy.

Fig. 1*A* demonstrates that the model captures the stress and temperature dependence of strain rate. To highlight the stress dependence of strain rate, we normalize the data to one temperature using our fitted activation energy in the inset of Fig. 1*A*. Although our model is not formally a power law, it gives an apparent power-law exponent of ~3.5 over the range of laboratory conditions, consistent with previous empirical analysis of this dataset (34).

Fig. 1*B* compares the predicted steady-state dislocation density with published measurements from experiments using single crystals of olivine (21–23). At intermediate applied stresses (30 to 400 MPa), the model predicts that the dislocation density approximates a power law of applied stress with an exponent of 1.4, consistent with an empirical power-law fit (22). However, at both small and large applied stress, the model predicts that dislocation density has a stronger dependence on applied stress, consistent with the trend of experimental data at small applied stresses and the more-limited data at large applied stresses. Aside from α, which relates the Taylor stress to the dislocation density, all parameters used to predict dislocation density are constrained by the calibration in Fig. 1*A*. The data in Fig. 1*B* constrains α to be 2.46 ± 0.13 (*SI Appendix*, Text). We note that the value of α only shifts the predicted dislocation-density curve in Fig. 1*B* to lower or higher dislocation density without affecting its shape.

We next calibrate the full model, including grain-size effects, against experimental data from Hansen et al. (35) and Keefner et al. (34). The former used fine-grained (≈10 μm) olivine aggregates. This calibration constrains the rate coefficients of the flow law Eq. **2** and both types of recovery Eq. **1**, as well as the activation energy. Fig. 1*C* compares the predicted grain-size dependence of strain rate against the experimental data. The experimental data are normalized to a single stress and

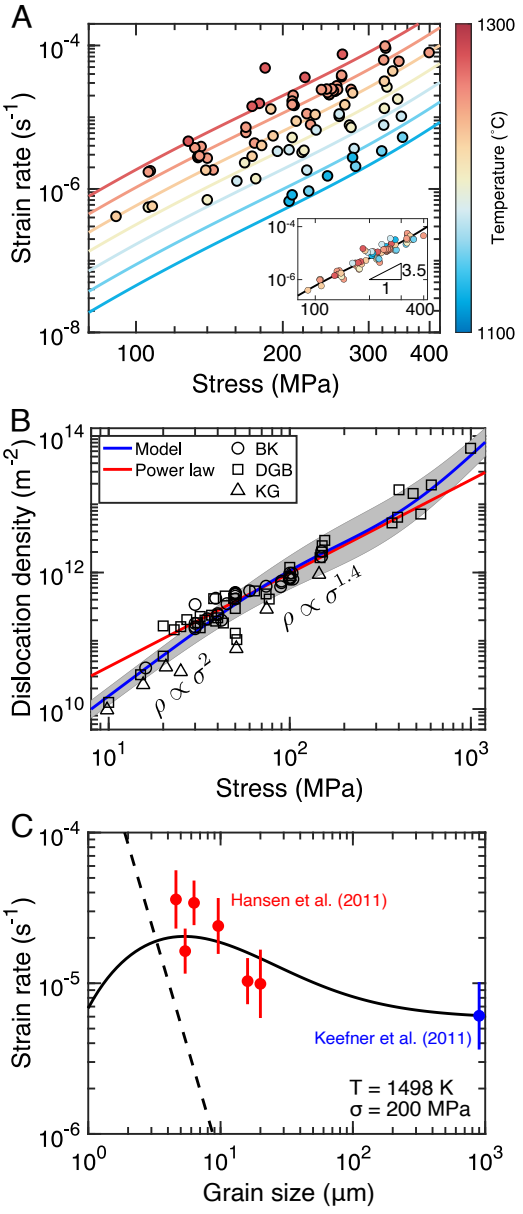

Fig. 1. Model predictions for steady-state deformation under laboratory conditions compared to experimental data. (*A*) Strain rate as a function of applied stress predicted by our calibrated model, assuming that grain-size effects are negligible (solid lines). The mechanical data from Keefner et al. (34) used in the calibration are plotted for comparison (circles) at different temperatures (indicated by color). The inset compares model prediction at T = 1,498 K with data normalized to this temperature. (*B*) Dislocation density as a function of stress predicted by the calibrated model plotted in *A* (blue line) compared to an empirical dislocation-density piezometer (22) (red line) and experimental data (black open symbols). The gray shaded area represents the 95% CI from propagating the uncertainties in the underlying model parameters. Data are taken from experiments on single crystals; BK = (22), DGB = (21), KG = (23). (*C*) Strain rate as a function of grain size predicted by the calibrated model incorporating grain-size effects (solid line) compared to normalized mechanical data from Keefner et al. (34) (blue) and Hansen et al. (35) (red). The experimental data are normalized to a temperature of 1,498 K and a stress of 200 MPa and then grouped according to grain size. The circles represent the mean normalized strain rate within each group. The error bars represent one SD of the normalized strain rate within each group. The strain rate predicted by the diffusion creep flow law from ref. 35 is plotted as a dashed line.

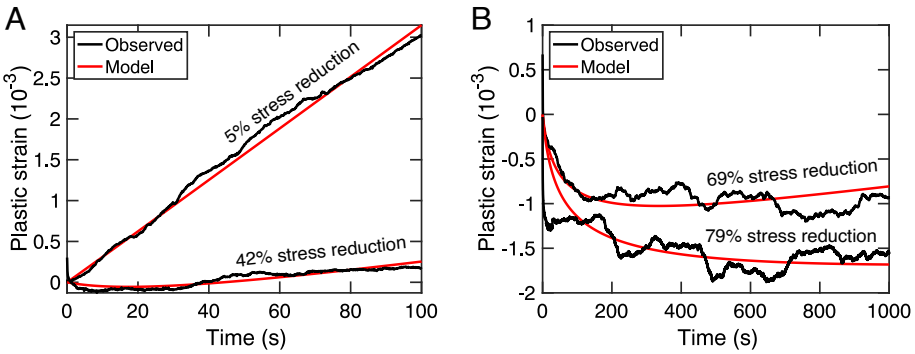

Fig. 2. Comparison of transient deformation predicted by our model to experimental data. Plastic strain as a function of time from a stress-reduction experiment (OxR0002) from Hansen et al. (6) (black line) compared to the model prediction (red line). This experiment was performed on a single crystal compressed uniaxially in the $[101]_c$ orientation at 1,523 K. The initial stress prior to reduction was 162 MPa. The curves are labeled with the percentage reduction in stress. In *A*, the plastic strain rate evolves over relatively short timescales (~10 s), whereas in *B*, the plastic strain rate evolves over longer timescales (~100 s).

temperature using the calibrated model. The calibrated model captures the stress, temperature, and grain-size dependencies of both datasets.

Finally, we consider the transient deformation predicted by our model. Hansen et al. (6) performed stress-reduction experiments in which olivine single crystals are deformed at a constant applied stress until steady-state deformation is achieved, and then, the applied stress is reduced to a new constant value. Transient deformation occurs after each stress step. We calibrate our model for single crystal deformation using steady-state mechanical data from Hansen et al., treating the steady-state Taylor stress prior to stress reduction as a fitting parameter (*SI Appendix*, Text). Fig. 2 demonstrates that our model provides a good fit to the transient plastic strain. Small stress reductions (<50%) lead to short transients, whereas larger stress reductions result in longer transients that have extended periods of reverse plastic strain rates. Importantly, our model is able to match the sense of the transient, in terms of forward or reverse plastic strain, as well as the magnitude of reverse plastic strain following the transient. In our model, the negative plastic strain rates result from the Taylor stress temporarily exceeding the (positive) applied stress, consistent with the Bauschinger effect.

Deformation in the Laboratory

Our model elucidates the microphysical relationships between dislocation density, applied stress, and strain rate that operate under laboratory conditions. The model illustrates that the steady-state dislocation density may be limited either by the Taylor stress or by recovery. In the first case, dislocation density increases until the Taylor stress approximately balances the applied stress, such that $\rho \propto \sigma^2$ and the strain rate becomes small. As a result, the dislocation storage rate becomes small and can balance the recovery rate. Alternatively, at steady state, the applied stress may significantly exceed the Taylor stress if dislocation density is limited instead by recovery. If recovery occurs mainly by pipe diffusion, the model predicts $\rho \propto \sigma^{2/3}$. The calibrated model predicts that, under laboratory conditions, both processes are significant, leading to the apparent $\rho \propto \sigma^{1.4}$ scaling observed in experimental data (Fig. 1*B*). This scaling previously lacked a physical explanation.

The ρ–σ scaling also influences the relationship between steady-state strain rate and applied stress. The steady-state strain rate is not linearly proportional to dislocation density as classically suggested by the Orowan equation (*SI Appendix*, Text) because the Taylor stress is also dependent on the dislocation density. The precise relationship between steady-state strain rate and dislocation density can be determined by solving Eq. **1** at steady state. If pipe-diffusion rate-limits dislocation climb, and thereby dislocation recovery, then $\dot{\varepsilon}_{ss} \propto \rho^{5/2}$. Combining this scaling for the strain rate with the scaling between dislocation density and applied stress under laboratory conditions, we predict an apparent stress exponent of $(5/2) \times 1.4 = 3.5$, in agreement with experimental data on coarse-grained olivine (Fig. 1*A*).

Accounting for grain-boundary processes results in a model that is sensitive to grain size, as illustrated in Fig. 1*C*. Grain size influences the steady-state dislocation density, and therefore strain rate, through recovery controlled by grain-boundary diffusion. Decreasing the grain size increases the rate of recovery, causing a corresponding decrease in the steady-state dislocation density and hence Taylor stress. At larger grain sizes, the strain rate is limited by the Taylor stress, and hence, the steady-state strain rate increases with decreasing grain size. However, at smaller grain sizes, the strain rate is instead limited by the availability of dislocations, and hence, further decreasing the grain size decreases the strain rate. At constant applied stress, the dependence of the steady-state strain rate on dislocation density can be understood through Eq. **2**, which has a maximum as a function of dislocation density.

These grain-size dependencies are consistent with available experimental data. For fine-grained samples (~10's μm) and laboratory-accessible stresses, our model predicts an inverse relationship between strain rate and grain size (Fig. 1*C*) and an approximate stress exponent of 3, congruent with empirical analyses (35). These data were previously interpreted in terms of dislocation-accommodated grain-boundary sliding (disGBS). In this interpretation, the strain rate is limited by dislocation annihilation at grain boundaries (37, 38). This rate-limiting process is the same as the case considered here, in which grain-boundary diffusion controls dislocation recovery. In classic models of disGBS, there is an additional contribution to the strain rate from sliding on grain boundaries, which we do not model. However, sliding is understood to make a limited contribution (1 to 10%) toward the total strain rate (39), justifying the omission of this process from our model. We note that recovery by grain-boundary diffusion has the same functional form as recovery due to grain-boundary migration, highlighting an additional link to models focused on migration as a recovery mechanism (36).

Deformation at Geological Strain Rates

We have thus far demonstrated consistency between our model and experiments. We now examine predictions of our model beyond laboratory conditions. In particular, we consider applied stresses far smaller than those normally accessed in the laboratory but typical within Earth's mantle. Fig. 3*A* explores the predicted dependence of strain rate on applied stress for a range of grain sizes. In the limit of infinite grain size, for which grain-boundary diffusion does not contribute to recovery, we predict a transition in stress exponent from 3.5 at typical laboratory stresses to 5 at smaller applied stresses. The transition in stress exponent results from a transition in the ρ–σ relationship.

As noted above, at small applied stresses, we predict $\rho \propto \sigma^2$ due to the reduced recovery rates associated with pipe diffusion. The recovery rate controls the difference between the applied stress and Taylor stress. At small applied stresses, the recovery rate becomes disproportionately small, such that the Taylor stress is approximately equal to the applied stress, resulting in the $\rho \propto \sigma^2$ scaling (Fig. 1*B*). Therefore, the apparent stress exponent is given by $(5/2) \times 2 = 5$. The range of predicted stress exponents for dislocation creep is consistent with the range of stress exponents observed in single-crystal deformation experiments performed on olivine, for which the stress exponent across experiments varied between 3 and 5 (42).

At finite grain size, the predicted steady-state strain rate curves in Fig. 3*A* have a complex relationship with the applied stress and grain size. Our model at steady state can be simplified by assuming that the applied stress balances the sum of the Taylor and threshold stresses, which approximately holds in Fig. 3*A*. Combining this balance with Eqs. **1** and **2** yields $\dot{\varepsilon}_{ss} \propto (\sigma - \sigma_d)^4(\sigma_d/\sigma)$. This approximate flow law has two limits. In the limit that $\sigma \gg \sigma_d$, we recover an apparent stress exponent of 3 and a grain size exponent of 1, consistent with observations in the laboratory (35). In the limit that $\sigma \to \sigma_d$, $\dot{\varepsilon} \to 0$ such that the threshold stress σ_d acts as a yield stress that is inversely proportional to the grain size, which is consistent with recent evaluations of the Hall–Petch effect (9).

The predicted scalings in Fig. 3*A* illustrate an important point. The measured power-law exponents describing relationships between steady-state strain rates, applied stresses, grain size, and dislocation density are not necessarily intrinsic properties of deformation mechanisms in a given material. Instead, empirical exponents reflect the underlying balance in microphysical processes under laboratory conditions. Therefore, exponents measured in the laboratory do not necessarily apply outside of these conditions, even though the same set of microphysical processes operate. Consequently, power laws fitted under laboratory conditions should only be extrapolated with extreme care. Furthermore, although we have considered only the effect of grain size and applied stress, the same considerations also apply to other state variables such as oxygen fugacity, water fugacity, and silica activity.

Fig. 3*B* is a deformation-mechanism map exploring the strain rate as a function of applied stress and grain size. We compare predicted strain rates to those derived from previous flow laws for dislocation creep (7) and grain-size sensitive dislocation creep (35). At typical laboratory strain rates ($\geq 10^{-5}\,s^{-1}$), the predictions of our calibrated model are in agreement with the previous flow laws. However, at mantle stresses ($\sim$ 1 MPa) and grain sizes ($\sim$3 mm) (19), the predicted strain rates are approximately an order of magnitude smaller than previous flow laws for dislocation deformation (7, 35). The difference in the predicted strength

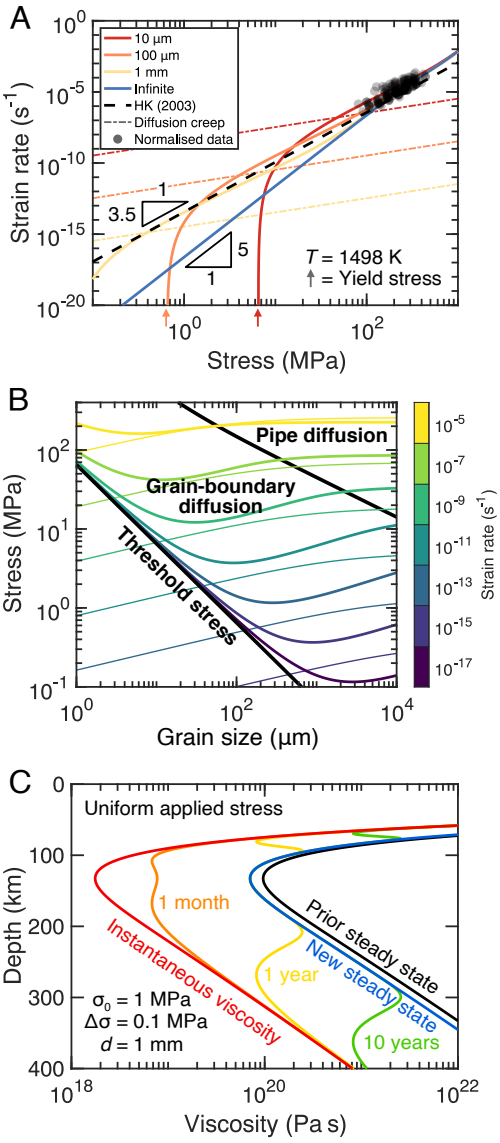

Fig. 3. Predictions of our calibrated model for deformation under geologic conditions. (*A*) Strain rate as a function of stress at a temperature of 1,498 K. Curves are constructed from the calibrated model incorporating grain-size effects using grain sizes of 10 µm, 100 µm, and 1 mm and from the calibrated model that neglects grain-size effects (infinite). Experimental data (black circles) from Keefner et al. (34) and Hansen et al. (35) are normalized to the same temperature using the fitted activation energy. Plotted for comparison are the dislocation-creep flow law (black dashed) from Hirth and Kohlstedt (7) and the diffusion-creep flow law (colored dot-dashed) from Hansen et al. (35). The yield stresses for dislocation deformation are indicated by arrows below the stress axis. (*B*) Deformation mechanism map of dislocation-accommodated deformation. The map is constructed as a function of grain size and stress at a temperature of 1,498 K. Contours represent a constant strain rate. Thick contours represent the strain rate predicted by our model, and the thin contours are calculated using a combination of the dislocation creep flow law from Hirth and Kohlstedt (7) and the grain-size sensitive dislocation creep flow law from Hansen et al. (35). The colors of the contours indicate the strain rate. The threshold stress and the boundary between the different dominant recovery mechanisms (pipe diffusion and grain-boundary diffusion) are plotted as thick black lines. (*C*) Viscosity as a function of depth predicted by our model assuming a mantle grain size of 1 mm. The initial steady-state viscosity under a uniform stress of 1 MPa is plotted as a black line. The colored lines indicate the viscosity following a 0.1-MPa increase in stress for a variety of times (red = instantaneous, orange = 1 mo following, yellow = 1 y following, green = 10 y following, blue = new steady state). The temperature as a function of depth is calculated assuming a half-space cooling model and an adiabatic geotherm for a 50 million-year-old lithosphere with a potential temperature of 1,350 °C (40, pp. 185–187). The activation volume is assumed to be 15 cm^3/mol in keeping with Dixon and Durham (41).

of the mantle reflects the changes in the scalings of the strain rate with applied stress and grain size predicted by our model outside of laboratory conditions. Indeed, our model predicts that deformation has a range of grain-size sensitivities, including both weakening and strengthening with decreasing grain size. Despite these differences, we find that our model at $d = 1$ mm and mantle stresses makes similar predictions to the Hirth and Kohlstedt (7) dislocation-creep flow law (Fig. 3*A*). This correspondence may explain the successful application of this dislocation creep flow law to geophysical models, e.g., ref. 43. Finally, a significant region of the deformation mechanism map corresponds to no deformation at all by dislocation-mediated mechanisms. In this region, stresses are lower than the threshold stress, although we note that typical mantle stresses and grain sizes lie outside this region. Deformation in this region is accommodated by other deformation mechanisms such as diffusion creep. The predictions of the diffusion-creep flow law from Hansen et al. (35) are compared to our model in Fig. 3*A*. The higher strain rates at low applied stress associated with high-temperature diffusion creep would obscure the yielding behavior predicted by our model.

Transient Deformation under Geological Conditions

Next, we consider the predictions of our model for time-dependent mantle deformation. Fig. 3*C* explores how an abrupt change in applied stress affects deformation under mantle conditions. We assume an initially uniform differential stress of 1 MPa, a reasonable ambient differential stress for the mantle (44). For this stress, the steady-state viscosity at 100 km depth is $\approx 10^{20}$ Pa s. Although the stress changes in realistic geodynamic processes will be spatially and temporally variable, in this simplified example, we apply a uniform stress change instantaneously, using a value consistent with stress changes inferred from models of postseismic creep (45). Although both the old and new steady-state viscosities are similar, the transient viscosities differ significantly from the steady state. Instantaneously, the viscosity drops by approximately two orders of magnitude (to $\approx 10^{18}$ Pa s at 100 km depth) and evolves over a timescale of months to years.

The large viscosity reduction instantaneously following a change in stress in Fig. 3*C* can be understood by examining Eq. **2**. At the instant of the stress change, the dislocation density is unchanged. Consequently, any change in viscosity must be controlled by the change in the net stress driving dislocation motion, which we term the effective stress. The ratio of viscosities immediately following (η^+) and prior to (η^-) the stress change are approximately given by

$$\frac{\eta^+}{\eta^-} \approx \frac{\sigma_{\text{eff}}^-}{\sigma_{\text{eff}}^- + \Delta\sigma}, \qquad [3]$$

where $\Delta\sigma$ is the stress change and $\sigma_{\text{eff}}^- = \sigma^- - \sigma_\rho - \sigma_d$ is the effective stress prior to the stress change. Under laboratory conditions, such as those considered in Fig. 2, the effective stress is inferred to be comparable in magnitude to the applied stress. As a result, stress changes will not drive disproportionate changes in the viscosity in laboratory experiments. However, under geological conditions, we predict that the steady-state effective stress is much smaller in magnitude than the applied stress, and thus, stress changes can drive disproportionate changes in the viscosity. Indeed, in Fig. 3C, the effective stress is predicted to be of the order of kPa, which is two orders of magnitude smaller than the stress change considered, and thus, the instantaneous transient viscosity is approximately two orders of magnitude smaller than the prior steady-state viscosity.

The magnitude of the reduction in viscosity and the evolution timescale are consistent with geophysical observations of processes associated with abrupt stress changes, such as postseismic creep (24, 43, 46) and crustal uplift in response to ongoing recent anthropogenic ice loss across a number of regions, e.g., refs. 47–50. The ratio of instantaneous to steady-state viscosity is approximately independent of depth, a prediction that is in striking agreement with viscosity profiles inverted from surface displacements after earthquakes (45). The rate of evolution toward steady state is depth dependent. Depths with smaller absolute transient viscosities, and therefore larger strain rates, evolve more quickly, indicating that dislocation storage controls the transient evolution of viscosity under mantle conditions. Thus, while steady-state deformation at mantle stresses is controlled by the recovery coefficients $\mathcal{R}_\times(T)$, transient deformation is sensitive to the flow law coefficient $A(T)$.

Transient, dislocation-accommodated deformation in Earth is commonly modeled using a nonlinear Burgers model, in which transient and steady-state viscosities possess the same sensitivity to the applied stress, e.g., ref. 6, and references therein. However, our results indicate that transient and steady-state viscosities have a fundamentally different dependence on the applied stress. Moreover, our results demonstrate that transient and steady-state viscosities under mantle conditions are likely controlled by separate components of the dislocation microphysics. In this work, we have considered the effect of dislocation density on transient deformation. Over comparable strains, transient deformation may also be influenced by other factors, such as the development of intergranular stress heterogeneity, e.g., ref. 51. However, models of this mechanism (51) assume nonlinear transient rheological laws that are in disagreement with laboratory observations, in which the initial strain-rates immediately following stress changes are a linear function of the new stress (6). Over strains larger than those investigated here, the evolution of other aspects of microstructure that we do not account for, such as grain size and crystallographic texture, will also influence the transient viscosity (52). Therefore, we suggest that the evolution of dislocation density is the most relevant process for predicting transient viscosity during stress changes that occur on human timescales, such as postseismic creep and crustal uplift in response to recent anthropogenic ice loss.

Broader Implications

Although we have calibrated our model for olivine deformation, our formulation is applicable to a broad array of materials. While the predicted transitions in stress exponent have not been directly observed in olivine, such transitions have been observed in solid-solution alloys (53), some of which have already been found to be good analogs for olivine (54). For example, in experiments on an Al–Mg alloy, the apparent stress exponent decreases from 5 to 3 for applied stresses above 7 MPa (55). This transition in stress exponent is correlated with a change in the scaling of an empirically-observed back stress opposing deformation, which we take to be the Taylor stress in our model. At the smallest stresses, for which the stress exponent is 5, the back stress is observed to be approximately equal to the applied stress, whereas at higher stresses, the back stress is a fraction of the applied stress (55). These observations are in agreement with the predictions of our model for olivine. We believe that this agreement underlines the importance of constructing microphysical models of deformation

to make physics-based predictions under conditions far from the laboratory.

The calibrated model that we have presented provides a quantitative description of dislocation creep, grain-size-sensitive dislocation creep, and the Hall–Petch effect in olivine. The model is in agreement with observations of transient strain obtained from stress-reduction tests and is in broad agreement with estimated transient viscosities from recent observations of geophysical processes associated with abrupt stress changes. Our model is easily extended to incorporate dynamic recovery (*SI Appendix*, Text), the dominant dislocation annihilation process at low temperatures. Indeed, our formulation of this process is consistent with that used by Hansen et al. (10) to model strain hardening and the Bauschinger effect at low temperatures. As a result, our model also extends to deformation by low-temperature plasticity. In this work, we have assumed that the activation energies of all processes are equal. Future work will constrain the potentially different activation energies of each process.

Data, Materials, and Software Availability. All data used in this work has been previously published in (6, 21–23, 34, 35). The data and code used in this work are available at: https://doi.org/10.5281/zenodo.7572686.

ACKNOWLEDGMENTS. T.B. was supported by a Natural Environment Research Council (NERC NE/L002612/1) studentship in the Oxford NERC Doctoral Training Partnership and by a Research Fellowship from the Royal Commission for the Exhibition of 1851. K.M.K. was supported by NSF grant EAR-1806791. L.N.H. and K.M.K. were supported by NSF grant EAR-2022433. This research received funding from the European Research Council under Horizon 2020 research and innovation program grant agreement number 772255. Lawrence Livermore National Laboratory is operated by Lawrence Livermore National Security, LLC, for the US Department of Energy, National Nuclear Security Administration under Contract DE-AC52-07NA27344. LLNL-JRNL-827673.

Author affiliations: [a]Department of Earth Sciences, University of Cambridge, Cambridge CB2 3EQ, UK; [b]Department of Earth Sciences, University of Oxford, Oxford OX1 3AN, UK; [c]Department of Earth and Environmental Sciences, University of Minnesota, Minneapolis, MN 55455; and [d]Lawrence Livermore National Laboratory, Livermore, CA 94550

1. M. Whittaker, W. Harrison, R. Lancaster, S. Williams, An analysis of modern creep lifing methodologies in the titanium alloy Ti6-4. *Mater. Sci. Eng.: A* **577**, 114–119 (2013).
2. B. Wilshire, P. Scharning, Prediction of long term creep data for forged 1Cr-1Mo-025v steel. *Mater. Sci. Technol.* **24**, 1–9 (2008).
3. B. M. Minchew, C. R. Meyer, A. A. Robel, G. H. Gudmundsson, M. Simons, Processes controlling the downstream evolution of ice rheology in glacier shear margins: Case study on rutford ice stream, West Antarctica. *J. Glaciol.* **64**, 583–594 (2018).
4. L. Pan *et al.*, Rapid postglacial rebound amplifies global sea level rise following West Antarctic ice sheet collapse. *Sci. Adv.* **7**, eabf7787 (2021).
5. S. Spigarelli, R. Sandström, Basic creep modelling of aluminium. *Mater. Sci. Eng.: A* **711**, 343–349 (2018).
6. L. N. Hansen, D. Wallis, T. Breithaupt, C. A. Thom, I. Kempton, Dislocation creep of olivine: Backstress evolution controls transient creep at high temperatures. *J. Geophys. Res.: Solid Earth* **126**, e2020JB021325 (2021).
7. G. Hirth, D. Kohlstedt, Rheology of the upper mantle and the mantle wedge: A view from the experimentalists. *Geophys. Monogr.-Am. Geophys. Union* **138**, 83–106 (2003).
8. W. Blum, P. Eisenlohr, F. Breutinger, Understanding creep–a review. *Metall. Mater. Trans. A* **33**, 291–303 (2002).
9. D. Dunstan, A. Bushby, Grain size dependence of the strength of metals: The Hall-Petch effect does not scale as the inverse square root of grain size. *Int. J. Plast.* **53**, 56–65 (2014).
10. L. N. Hansen *et al.*, Low-temperature plasticity in olivine: Grain size, strain hardening, and the strength of the lithosphere. *J. Geophys. Res.: Solid Earth* **124**, 5427–5449 (2019).
11. U. Kocks, A statistical theory of flow stress and work-hardening. *Philos. Mag.* **13**, 541–566 (1966).
12. U. F. Kocks, Laws for work-hardening and low-temperature creep. *J. Eng. Mater. Technol.* **98**, 76–85 (1976).
13. U. Essmann, H. Mughrabi, Annihilation of dislocations during tensile and cyclic deformation and limits of dislocation densities. *Philos. Mag. A* **40**, 731–756 (1979).
14. H. Mecking, U. Kocks, Kinetics of flow and strain-hardening. *Acta Metall.* **29**, 1865–1875 (1981).
15. Y. Estrin, H. Mecking, A unified phenomenological description of work hardening and creep based on one-parameter models. *Acta Metall.* **32**, 57–70 (1984).
16. Y. Estrin, Dislocation theory based constitutive modelling: Foundations and applications. *J. Mater. Process. Technol.* **80**, 33–39 (1998).
17. W. Nix, J. Gibeling, D. Hughes, Time-dependent deformation of metals. *Metall. Trans. A* **16**, 2215–2226 (1985).
18. R. Sandström, J. Hallgren, The role of creep in stress strain curves for copper. *J. Nucl. Mater.* **422**, 51–57 (2012).
19. G. Hirth, D. Kohlstedt, The stress dependence of olivine creep rate: Implications for extrapolation of lab data and interpretation of recrystallized grain size. *Earth Planet. Sci. Lett.* **418**, 20–26 (2015).
20. D. Kohlstedt, C. Goetze, W. Durham, J. Vander Sande, New technique for decorating dislocations in olivine. *Science* **191**, 1045–1046 (1976).
21. W. Durham, C. Goetze, B. Blake, Plastic flow of oriented single crystals of olivine: 2. Observations and interpretations of the dislocation structures. *J. Geophys. Res.* **82**, 5755–5770 (1977).
22. Q. Bai, D. Kohlstedt, High-temperature creep of olivine single crystals, 2. dislocation structures. *Tectonophysics* **206**, 1–29 (1992).
23. D. Kohlstedt, C. Goetze, Low-stress high-temperature creep in olivine single crystals. *J. Geophys. Res.* **79**, 2045–2051 (1974).
24. A. M. Freed, G. Hirth, M. D. Behn, Using short-term postseismic displacements to infer the ambient deformation conditions of the upper mantle. *J. Geophys. Res.: Solid Earth* **117**, B01409 (2012).
25. W. Blum, Role of dislocation annihilation during steady-state deformation. *Phys. Status Solidi (b)* **45**, 561–571 (1971).
26. J. Spingarn, D. Barnett, W. Nix, Theoretical descriptions of climb controlled steady state creep at high and intermediate temperatures. *Acta Metall.* **27**, 1549–1561 (1979).
27. J. Spingarn, W. Nix, A model for creep based on the climb of dislocations at grain boundaries. *Acta Metall.* **27**, 171–177 (1979).
28. E. Hart, On the role of dislocations in bulk diffusion. *Acta Metall.* **5**, 597 (1957).
29. E. Orowan, Zur kristallplastizität. i. *Z. Für Phys.* **89**, 605–613 (1934).
30. A. Krausz, A rate theory of dislocation mobility. *Acta Metall.* **16**, 897–902 (1968).
31. G. I. Taylor, The mechanism of plastic deformation of crystals. part i.–theoretical. *Proc. R. Soc. London. Ser. A, Containing Pap. Math. Phys. Charact.* **145**, 362–387 (1934).
32. T. T. Gribb, R. F. Cooper, Low-frequency shear attenuation in polycrystalline olivine: Grain boundary diffusion and the physical significance of the andrade model for viscoelastic rheology. *J. Geophys. Res.: Solid Earth* **103**, 27267–27279 (1998).
33. S. Karato, *Deformation of Earth Materials: An introduction to the Rheology of Solid Earth* (Cambridge University Press, 2008), p. 158.
34. J. Keefner, S. Mackwell, D. Kohlstedt, F. Heidelbach, Dependence of dislocation creep of dunite on oxygen fugacity: Implications for viscosity variations in earth's mantle. *J. Geophys. Res.: Solid Earth* **116**, B05201 (2011).
35. L. Hansen, M. Zimmerman, D. L. Kohlstedt, Grain boundary sliding in San Carlos olivine: Flow law parameters and crystallographic-preferred orientation. *J. Geophys. Res.: Solid Earth* **116**, B08201 (2011).
36. J. Platt, W. Behr, Grainsize evolution in ductile shear zones: Implications for strain localization and the strength of the lithosphere. *J. Struct. Geol.* **33**, 537–550 (2011).
37. T. Langdon, A unified approach to grain boundary sliding in creep and superplasticity. *Acta Metall. Mater.* **42**, 2437–2443 (1994).
38. F. Ferreira, L. N. Hansen, K. Marquardt, The effect of grain boundaries on plastic deformation of olivine. *J. Geophys. Res.: Solid Earth* **126**, e2020JB020273 (2021).
39. T. G. Langdon, Grain boundary sliding revisited: Developments in sliding over four decades. *J. Mater. Sci.* **41**, 597–609 (2006).
40. D. L. Turcotte, G. Schubert, Geodynamics (Cambridge University Press, 2002), pp. 185–187.
41. N. A. Dixon, W. B. Durham, Measurement of activation volume for creep of dry olivine at upper-mantle conditions. *J. Geophys. Res.: Solid Earth* **123**, 8459–8473 (2018).
42. Q. Bai, S. Mackwell, D. Kohlstedt, High-temperature creep of olivine single crystals 1. mechanical results for buffered samples. *J. Geophys. Res.: Solid Earth* **96**, 2441–2463 (1991).
43. A. M. Freed, R. Bürgmann, Evidence of power-law flow in the Mojave desert mantle. *Nature* **430**, 548–551 (2004).
44. L. Kohlstedt, L. Hansen, "Constitutive equations, rheological behavior, and viscosity of rocks" in *Mineral Physics. Treatise on Geophysics* (ed. price, gd, stixrude, l.) 2 (2015).
45. J. R. Weiss *et al.*, Illuminating subduction zone rheological properties in the wake of a giant earthquake. *Sci. Adv.* **5**, eaax6720 (2019).
46. A. M. Freed, R. Bürgmann, E. Calais, J. Freymueller, S. Hreinsdóttir, Implications of deformation following the 2002 Denali, Alaska, earthquake for postseismic relaxation processes and lithospheric rheology. *J. Geophys. Res.: Solid Earth* **111**, B01401 (2006).
47. V. R. Barletta *et al.*, Observed rapid bedrock uplift in Amundsen Sea Embayment promotes ice-sheet stability. *Science* **360**, 1335–1339 (2018).
48. S. A. Khan *et al.*, Geodetic measurements reveal similarities between post-last glacial maximum and present-day mass loss from the greenland ice sheet. *Sci. Adv.* **2**, e1600931 (2016).
49. A. Richter *et al.*, Crustal deformation across the southern patagonian icefield observed by GNSS. *Earth Planet. Sci. Lett.* **452**, 206–215 (2016).
50. C. F. Larsen, R. J. Motyka, J. T. Freymueller, K. A. Echelmeyer, E. R. Ivins, Rapid viscoelastic uplift in southeast Alaska caused by post-little ice age glacial retreat. *Earth Planet. Sci. Lett.* **237**, 548–560 (2005).
51. Si. Karato, A theory of inter-granular transient dislocation creep: Implications for the geophysical studies on mantle rheology. *J. Geophys. Res.: Solid Earth* **126**, e2021JB022763 (2021).
52. L. Hansen, M. Zimmerman, D. Kohlstedt, Laboratory measurements of the viscous anisotropy of olivine aggregates. *Nature* **492**, 415–418 (2012).
53. P. Yavari, T. G. Langdon, An examination of the breakdown in creep by viscous glide in solid solution alloys at high stress levels. *Acta Metall.* **30**, 2181–2196 (1982).
54. R. F. Cooper, D. S. Stone, T. Plookphol, Load relaxation of olivine single crystals. *J. Geophys. Res.: Solid Earth* **121**, 7193–7210 (2016).
55. H. Oikawa, K. Sugawara, S. Karashima, Creep behavior of al-2.2 at% mg alloy at 573 k. *Trans. Jpn. Inst. Met.* **19**, 611–616 (1978).